Published online 29 April 2020

Nucleic Acids Research, 2020, Vol. 48, No. 10 ***e60***
doi: 10.1093/nar/gkaa250

A proteinase-free DNA replication machinery for *in vitro* and *in vivo* amplified MicroRNA imaging

Jie Wei, Huimin Wang, Xue Gong, Qing Wang, Hong Wang, Yangjie Zhou and Fuan Wang*

Key Laboratory of Analytical Chemistry for Biology and Medicine (Ministry of Education), College of Chemistry and Molecular Sciences, Wuhan University, Wuhan 430000, P. R. China

Received December 09, 2019; Revised March 05, 2020; Editorial Decision March 30, 2020; Accepted April 01, 2020

ABSTRACT

The construction of robust, modular and compact DNA machinery facilitates us to build more intelligent and ingenious sensing strategies in complex biological systems. However, the performance of conventional DNA amplifiers is always impeded by their limited in-depth amplifications and miscellaneously enzymatic requirements. Here, a proteinase-free reciprocal DNA replication machinery is developed by exploiting the synergistic cross-activation between hybridization chain reaction (HCR) and DNAzyme. The DNAzyme provides an efficient way to simplify the sophisticated design of HCR machinery and simultaneously to promote the amplification capacity. And the HCR-assembled tandem DNAzyme nanowires produce numerous new triggers for reversely stimulating HCR amplifier as systematically explored by experiments and computer-aided simulations. The reciprocal amplifier can be executed as a versatile and powerful sensing platform for analyzing miRNA in living cells and even in mice, originating from the inherent reaction accelerations and multiple-guaranteed recognitions. The reciprocal catalytic DNA machine holds great potential in clinical diagnosis and assessment.

INTRODUCTION

The development of isothermal autonomous nucleic acid amplification systems attracted substantial research interests (1–3) owing to their extensive applications in clinical diagnosis, food security, environmental monitoring and forensic analysis (4,5). Based on the different catalytic reaction mechanisms, these strategies could be mainly classified as enzymatic and nonenzymatic proteinase-free amplification machineries. These different enzyme-catalyzed machineries have been initially employed to amplify nucleic acid, including rolling circle amplification (RCA) (6), loop-mediated isothermal amplification (LAMP) (7) and strand-displacement amplification (SDA) (8). However, the effectiveness of these enzyme-catalyzed machineries usually relies on certain protein enzymes that might be susceptible to the delicate interference of external environment. Thus, it is highly desirable to develop more robust and convenient sensing strategies for the complicated biological environment.

Recently, a fascinating group of proteinase-free catalytic machineries was developed for *in vitro* and *in vivo* nucleic acid amplification. These versatile proteinase-free sensing strategies hold great promise in clinical diagnosis of low-expression biomarkers owing to their convenient design, robust execution, and high signal gain. And these included DNAzyme-catalyzed machineries (9) and cascaded hybridization-based machineries (10). DNAzymes are catalytic nucleic acids that have been recognized as attractive amplifying labels for various biosensing events (11–15). DNAzyme-catalyzed machineries were accomplished by the activation of the isothermal DNAzyme-based catabolism or anabolism process in solution (14,16) and on surfaces (17,18). However, the amplification performance of these different DNAzyme platforms is constrained by their inherent low catalytic efficiency. As a characteristic hybridization cascading machinery, HCR has been recently developed with low signal leakage (19–21). HCR provides a facile amplification mean for analyzing various nucleic acid analytes on cell surfaces as well as inside living cells (22–25). HCR involves an efficient analyte-triggered successive cross-opening of hairpin reactants for generating nicked dsDNA copolymers (19). However, the relatively low reaction velocity of HCR system results in an unsatisfying signal amplification efficiency for analyzing biomarkers of trace amount which is especially appealing in earlier clinical diagnosis. To address this issue, HCR was further integrated with other amplification procedures through a traditional stacked configuration, and achieved an improved sensing performance (26–31). Yet these concatenated systems are still hindered by their low amplification depth and efficiency.

The reciprocal catalytic DNA machinery is thus proposed as the theoretically most efficient multi-series amplification system in which the reciprocal partners could reinforce mutually each other through the exquisite cross-

*To whom correspondence should be addressed. Tel: +86 27 68756307; Fax: +86 27 68756307; Email: fuanwang@whu.edu.cn

catalytic pathways. The trigger could be autonomously supplemented for accelerating the reciprocal catalytic reaction processes. Through the increasing accumulation of triggers, the advanced reciprocal catalytic amplifiers could substantially promote the reaction accomplishment until exhausting all reactants. These enzymatic reciprocal catalytic DNA amplification systems have been extensively developed for *in vitro* bioanalysis (32–34), while rare interests are spent on the proteinase-free reciprocal catalytic amplifier machinery for *in vivo* analysis (35,36). This might be attributed to their inherently and distinctly different transducing interfaces that require an extremely sophisticated design for signal translations and integrations. Moreover, the heterogeneous reciprocal cross-catalytic circuits can significantly contribute to the reliable bioanalysis due to their multiple-guaranteed molecular recognitions and successively accelerated molecular reactions. The performance of DNAzyme machines was promoted by anchoring DNAzyme walkers on surfaces, where the localized DNAzyme biocatalytic reaction could substantially promote the successive RNA-cleaving reaction (17,18). The DNAzyme amplifiers have been also extensively developed by its integration with other amplification means, including HCR and CHA amplifiers (37–39). Yet the depth of these integration is limited for not considering the reverse DNAzyme, HCR and CHA feedback approaches. It is expected that the amplification capacity of DNAzyme could be remarkably enhanced by the HCR-mediated cross-catalysis, thus significantly accelerating the entire reciprocal DNAzyme amplification process. Especially, the rational assembly of DNAzyme and HCR modules could contribute to the ingenious construction of a reciprocal DNA amplifier by integrating the flexibility and reliability of each machinery constitute. Besides, the proteinase-free reciprocal DNAzyme amplification machinery is rarely explored for intracellular or *in vivo* miRNA imaging. We have recently reported an autocatalytic DNAzyme biocircuit for intracellular miR-21 imaging where an additional MnO_2 nanoparticle is introduced as DNAzyme cofactor suppliers and DNA probes carriers (40) since the accessible Mn^{2+} ions are inadequate to realize an efficient DNAzyme biocatalysis in living cells. The as-introduced MnO_2 also revealed a comparably lower biocompatibility and essentially lower DNA loading capacity, which required more experimental optimization to guarantee a delicate balance between the supply of adequate DNAyzme cofactors and sufficient DNA delivering carriers. Noted that the unexpected adverse retention of transfecting inorganic nanomaterials *in vivo* might bring unexpected biotoxicity, which remains the critical limitations for their extensive biological applications. Due to their intrinsic good biocompatibility and essential high DNA loading capacity, the commercial facile transfection agents have emerged as an attractive candidate for delivering various DNA probes into living cells/tissues (24,41). Moreover, the DNAzyme amplifier is not a versatile and generalized biosensing platform since all DNA probes need to be completely redesigned to detect another analyte. And the MnO_2-based DNAzyme system is mainly based on experimental research without in-depth exploration into their reaction procedure at single-molecular level, which is especially appealing for explicating and facilitating the more advanced design of DNA and DNAzyme circuits.

Herein, we develop a proteinase-free and nanomaterials-free replicating HCR (R-HCR) machinery based on the cross-invasion of HCR and DNAzyme biocatalysis. The DNAzyme and HCR were adapted for the elaborate assembly of a reciprocal catalytic amplifier. The sophisticated design and limited amplification of traditional HCR could be substantially eliminated by using the DNAzyme amplifying mediator. Target activates an autonomous and continuous cross-opening of metastable hairpins in HCR amplifier, leading to the assembly of tandem DNAzyme concatemers. The as-achieved DNAzyme then catalyzes the consecutive cleavage of substrate that supplements new targets for reversely feeding back the HCR transducer. Based on the facile DNAzyme cofactors supply of endogenous Mg^{2+} ions and the commercial transfection agent, our DNAzyme amplification method is simple and easy-to-operate. Based on the DNAzyme-sustained accumulation of HCR trigger and the reverse HCR-facilitated activation of DNAzyme, this reciprocal catalytic procedure leads to a remarkably amplified transduction of the molecular recognition process as systematically explored by experiments and computer-aided simulations. The versatile R-HCR amplifier was further examined as a general and robust sensing module for *in vitro* detection and *in vivo* imaging of different microRNAs with the aid of an auxiliary sensing module. The present nanomaterial-free DNAzyme amplifier represents a biocompatible system by preventing the inevitable exposure and the unexpected adverse retention of transfecting nanomaterials. Our unprecedented R-HCR imaging system achieves a reliable signal localization of miRNA in living cells and mice, thus holding great promise for *in vivo* detecting trace amount of biomarkers in cell biology and clinical diagnosis.

MATERIALS AND METHODS

Materials

4-(2-Hydroxyethyl)piperazine-1 ethanesulfonic acid sodium salt (HEPES), magnesium chloride and sodium chloride were of analytical grade and were purchased from Sigma-Aldrich (MO, USA) unless otherwise indicated. DNA marker and GelRed were purchased from Invitrogen (Carlsbad, CA, USA). All oligonucleotides (Supplementary Tables S1–S3, Supporting Information) were custom-designed and then synthesized by Sangon Biotech. Co., Ltd (Shanghai, China). They were HPLC-purified by the company and further PAGE-purified prior to experiment in lab. Fetal bovine serum (FBS), Lipofectamine 3000 transfection Reagent, Dulbecco's modified Eagle's medium (DMEM) was purchased from HyClone (Logan, UT, USA). Trypsin and Penicillin-streptomycin were purchased from Genview (USA). 3-(4,5-Dimethylthiazol-2-yl)-2,5 diphenyltetrazolium bromide (MTT) was purchased from Beyotime Institute of Biotechnology (Shanghai, China). MCF-7, A549, MRC-5 and HeLa cells were obtained from Shanghai Institutes for Biological Sciences (SIBS). Human serum samples were kindly donated by healthy volunteers. All solutions were prepared using ultrapure water, which

was obtained through a Milli-Q water purification system with an electric resistance >18.2 MΩ·cm. Atomic force microscope (AFM) cantilever (SCANASYST-AIR) was purchased from Bruker (Camarilla, CA, USA).

Fluorescence assay

Unless specifically presented, all of control experiments were carried out without changing the concentrations of specific DNA reactants except subtracting or replacing the undesired oligonucleotides from their respective reactants. For amplified analysis of DNA by using R-HCR and HCR amplifiers, the target was incubated with their respective DNA mixtures (H_1+H_2+H_3+H_4+S_M+L for HCR, and H_1+H_2+H_3+H_4+S+L for R-HCR amplifier, 200 nM each) for 3 h at 25°C unless specified. For sensitive miR-21 or miR-155 assay by the updated R-HCR circuit, the target (miR-21 or miR-155) was added into the mixture of 'helper' hairpin (H_5 or H_6) (100 nM) and R-HCR reactants (H_1+H_2+H_3+H_4+S+L, 200 nM each) at 25°C for 3 h unless specified. The real-time fluorescence monitoring of R-HCR machine and its controls were implemented by using a Cary Eclipse spectrometer (Varian Inc) at 25°C. The fluorescence spectra were collected from 505 to 650 nm upon exciting these samples at 490 nm. The time-dependent fluorescence change is recorded at the emission wavelength of 520 nm and F_0 represents the original fluorescence intensity.

Native polyacrylamide gel electrophoresis

Gel electrophoresis was performed to verify the working principle of R-HCR system, 50 nM of target **T** was mixed with 200 nM of their DNA reactants (H_1+H_2+H_3+H_4+S_M+L for HCR, and H_1+H_2+H_3+H_4+S+L for R-HCR amplifier) in reaction buffer (10 mM HEPES, 1 M NaCl, 50 mM $MgCl_2$, pH 7.2) for 3 h at 25°C. Then all samples were added into the freshly prepared native polyacrylamide (12%) gel matrix. Electrophoresis was implemented at 120 V in 1× TBE buffer (89 mM Tris, 89 mM boric acid, 2.0 mM EDTA, pH 8.3) for 3 h. After staining in diluted GelRed™ solution for 20 min, the gel was imaged by FluorChem FC3 (ProteinSimple, USA) under 365 nm UV irradiation.

Atomic force microscope (AFM) characterization

AFM characterization was carried out to verify the R-HCR-generated linear dsDNA nanowires. Here, 20 nM of target (**T**) was incubated with 200 nM of reactants (H_1+H_2+H_3+H_4+S+L) in reaction buffer (10 mM HEPES, 1 M NaCl, 50 mM $MgCl_2$, pH 7.2) for 3 h at 25°C unless specified. The freshly cleaved mica was reacted with 1 M of Mg^{2+} ions for 15 min. These diluted DNA samples were deposited on the modified mica for 15 min, followed by its rinsing with deionized water. The dried sample was scanned in tapping mode by Multimode 8 Atomic Force Microscope with a NanoScope V controller (Bruker Inc.). The silicon tips used for AFM analysis were SCANASYST-AIR (tip radius: ∼2 nm; resonance frequency: ∼70 kHz; spring constant: ∼0.4 N/m; length: 115 μm; width: 25 μm).

Intracellular R-HCR-imaging experiment

MCF-7, A549, HeLa and MRC-5 cells were cultured in DMEM medium containing 10% FBS and 1% penicillin/streptomycin in 5% CO_2 atmosphere at 37°C. All cells above were plated in glass bottom culture dishes and grown to 70% confluency for 12 h for the following transfection. Briefly, the miR-21-targeting R-HCR mixture containing H_5 (0.05 nmol) and H_1+H_2+H_3+H_4+S+L (0.1 nmol each) in Opti-MEM (200 μl) was mixed with lipofectamine 3000 (5 μl) in Opti-MEM (200 μl) for 5 min. Then the above Opti-MEM transfection mixture and a supplementary 80 μl of FBS were introduced into the plated cells for 4 h at 37°C. Subsequently, the cultured cells were washed three times with phosphate buffered saline (PBS) and cultured in DMEM medium (1.0 ml) containing 10% FBS for confocal imaging. When implementing the anti-miRNA antisense inhibitor oligonucleotide experiment, MCF-7 cells were transfected with inhibitor oligonucleotide (0.1 nmol) using lipofectamine 3000 (3 μl) for 2 h, and were subsequently transfected and incubated with the R-HCR imaging system for 4 h. The detection of miR-155 is the same as that of miR-21.

Confocal laser scanning microscopy (CLSM) characterization

All cellular fluorescence images were obtained by Leica TCS-SP8 laser scanning confocal microscopy system. A series of FRET, donor and acceptor filters were utilized to collect the following fluorescence readout: donor fluorescence (FAM), acceptor fluorescence (TAMRA) from FRET and external excitation. Upon exciting the system with 488 nm, the fluorescence emission spectra were collected from 500 to 560 nm for green channel of fluorophore donor (FAM), and the FRET-generated fluorescence emission spectra was collected from 575 to 635 nm for yellow channel of fluorophore acceptor (TAMRA). Upon exciting the system with 561 nm, the external excited fluorescence emission spectra were collected from 575 to 635 nm for red channel of fluorophore acceptor (TAMRA). All images were developed at 63.0 × 1.40 objective with oil. The fluorescence emission ratio of acceptor to donor (F_A/F_D) was denoted as the FRET signal for intracellular imaging upon exciting the R-HCR imaging system with 488 nm. The respective fluorescence (F_A and F_D) signals of different cells were obtained by integrating the fluorescence image of each sample. To get a reliable quantitative FRET signal, the background FRET signal, originating from FAM or TAMRA fluorophore itself, was deducted from each sample. All FRET images were analyzed and processed by using ImageJ software.

Live animal imaging

Balb/c nude mice (4–6 weeks old) were subcutaneously injected with 5×10^6 cells on the right side of the back. Tumor volume was analyzed using the following equation: $V = (L \times W^2)\pi/6$ (L and W are the longest and shortest diameters of the tumor, respectively). When the tumors reach to the size of 100 mm^3, the mice were randomly divided into four groups for the treatment with lipo3000-loaded R-HCR (H_1+$H_2^{\#}$+H_3+$H_4^{\#}$+S+L, 5 nmol/kg each,

H_5, 2.5 nmol/kg), HCR (H_1+$H_2^{\#}$+H_3+$H_4^{\#}$+S_M+L, 5 nmol/kg each, H_5, 2.5 nmol/kg), H_5-expelled R-HCR (H_1+$H_2^{\#}$+H_3+$H_4^{\#}$+S+L, 5 nmol/kg each) and R-HCR with a chemically modified miR-21 inhibitor (miR-21 inhibitor, H_1+$H_2^{\#}$+H_3+$H_4^{\#}$+S+L, 5 nmol/kg each, H_5, 2.5 nmol/kg) through intratumoral or intravenous injection. Mice were imaged using PE Spectrum & Quantum FX at 0, 3, 6, 9 h after intratumoral injection and at 4, 8, 12 h after intravenous injection with excitation and emission wavelengths of 640 and 680 nm, respectively. Then they were sacrificed to collect the major organs and tumors for *ex vivo* imaging. Animal experiments were approved by the Animal Care and Use Committee of Wuhan University.

RESULTS

Principle of R-HCR machinery

The present R-HCR amplification platform is based on the design of appropriate HCR hairpin reactants (**H_1**, **H_2**, **H_3** and **H_4**) that are grafted with DNAzyme subunits, and an additional DNAzyme substrate hybrid (partially hybridized **S**/**L** duplex) that is functionalized with the initiator sequence (Figure 1). The initiator activates the cross-hybridization of HCR hairpins to generate long nicked dsDNA nanowires that carry chains of tandem RNA-cleaving E6-type DNAzymes (42). The HCR-assembled DNAzymes then catalyze the efficient cleavage of DNAzyme substrate, releasing numerous initiator sequence for reversely triggering the HCR amplifier. As shown in Figure 1A, the respective functionalization of DNAzyme subunits into the separated hairpins (**H_1** and **H_3**) prohibits the formation of an active DNAzyme while the different fluorophore-labelled hairpins (**H_2** and **H_4**) prohibits their efficient FRET procedure. The substrate (**S**), consisting of a ribonucleotide (rA)-containing DNAzyme substrate a*–h* and an initiator sequence (**T**), hybridizes partially with the blocker strand (**L**) to prohibit the undesired HCR-motivated signal leakage. The analyte (**T**) triggers the cyclic cross-opening of HCR reactants, leading to a sustained assembly of DNAzyme nanowires that bring the two fluorophores (FAM and TAMRA) into close proximity, thus enabling the Förster resonance energy transfer (FRET) process. Subsequently, each DNAzyme can catalyze the continuous scission of the substrate hybrid (**S**/**L**) to release new trigger strands for reversely stimulating the HCR transducer. During this reciprocal catalytic process, each HCR-mediated **H_2**–**H_4** hybridization event generates one FRET signal and each concomitant **H_1**–**H_3** hybridization event generates one active DNAzyme unit. Noted that each of these assembled DNAzymes produces substantial amount of HCR triggers for accelerating the whole reciprocal catalytic reaction process. The amplifcation efficiency of conventional HCR and DNAzyme amplifers was simplified as N, then the newly developed R-HCR amplifier shows an exponential amplification efficiency ($1:N^N$) based on the reciprocal catalytic accumulation of HCR triggers and DNAzyme units. This leads to the promoted assembly of long tandem DNAzyme nanowires and the enhanced generation of FRET signal (detailed sequence, see Supplementary Table S1).

Feasibility study of the R-HCR machinery

For this proof-of-concept study, the as-achieved R-HCR amplifier as illustrated in Figure 1A was first examined under optimal conditions (43) (Supplementary Figures S1 and S2). As expected, the R-HCR mixture shows no fluorescence change without initiator (Figure 2A), indicating these DNA probes are metastable without obvious signal leakage (spontaneous reciprocal cross-catalytic reactions). However, when initiator **I** was introduced into the R-HCR mixture, a dramatical fluorescence change was revealed and it leveled off after 1.5 h (Figure 2A). More control experiments were carried out for examining the detailed working mechanism of the R-HCR amplifier. Firstly, the indispensable role of HCR system was investigated by removing one of the non-fluorescent hairpins (**H_1** or **H_3**) from the HCR system. Obviously, the **H_1**- or **H_3**-excluded R-HCR amplifier disables the HCR-motivated dsDNA assembly and FRET generation (curves b, d of Figure 2B). These observations demonstrated that all participating HCR hairpins are indispensable to propagate the HCR-amplified FRET signal generation. Besides HCR, the DNAzyme biocatalysis was then explored by replacing the adenine ribonucleotide of substrate (**S**) with an adenine deoxynucleotide, resulting in the generation of a mutant substrate (**S_M**) that could not be cleaved by DNAzyme. A comparably lower fluorescence response was obtained for the **S_M**-substituted R-HCR machine (a characteristic traditional HCR amplifier) upon its incubation with analyte (curve f of Figure 2B). Here the HCR-assembled DNAzyme could not cleave the mutant **S_M** for triggering HCR system. This blocked DNAzyme-catalyzed HCR assembly leads to the assembly of a conventional HCR amplifier. As expected, a dramatic fluorescence response was observed for the R-HCR machinery (curve h of Figure 2B), which is ascribed to the HCR-generated tandem DNAzyme copolymers that activate the production of initiators for feeding back HCR system. The newly developed R-HCR amplifier shows an exponential amplification efficiency ($1:N^N$), which is substantially higher than the multiple amplification efficiency (1:N) of conventional HCR. These results clearly demonstrate the successful coupling of HCR and DNAzyme without signal leakage, and the hierarchical integration of our reciprocal catalytic amplifier with significant signal gain.

Native gel electrophoresis and atomic force microscopy (AFM) experiments were then carried out to explicit the detailed reaction procedure of our R-HCR amplifier. The **S_M**-substituted R-HCR system was examined as conventional HCR amplifier. As indicated in Figure 2C, more bulky HCR products appeared for the target-activated R-HCR system (sample ix) than that of the **S_M**-substituted conventional HCR system (sample xiii), owing to the consecutive accumulation of triggers for accelerating HCR system. This promoted dsDNA assembly also implies a significant amplification capability of our reciprocal reaction process. Besides, the band of substrate hybrid (**S**/**L**) became faint and even disappeared, while new product band of the cleaved substrate emerged for the target-activated R-HCR system (sample ix). Meanwhile, the band of mutant substrate hybrid (**S_M**/**L**) remained unchanged without generating new product band of the cleaved substrate for the mu-

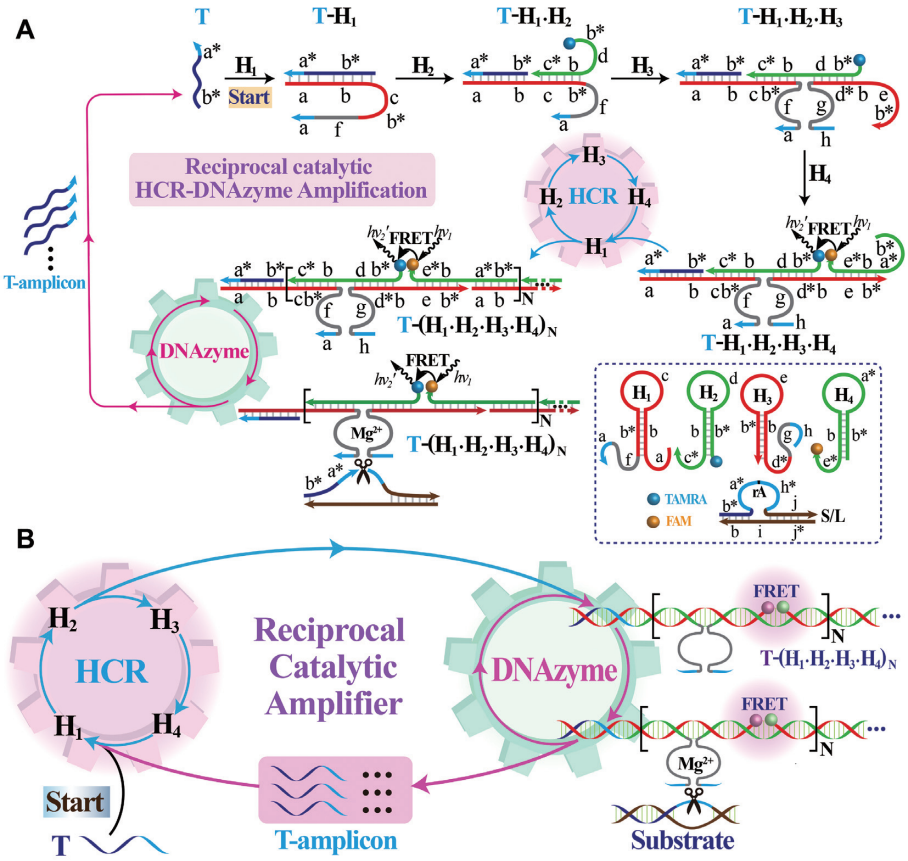

Figure 1. (**A**) Scheme reaction procedure of the proteinase-free replicating catalytic DNA machinery consisting of hybridization chain reaction (HCR) and DNAzyme biocatalysis. (**B**) Simplified representation of the reciprocal HCR (R-HCR) amplification machinery.

tant $\mathbf{S_M}$-substituted HCR system (sample xiii). This was attributed to the mutant substrate $\mathbf{S_M}$ with adenine deoxynucleotide which could not be cleaved by the present RNA-cleaving DNAzyme. Only the substrate (**S**) with adenine ribonucleotide could be be cleaved by the RNA-cleaving DNAzyme. In addition, the catalyzed cleavage of mere substrate (**S**) by HCR-assembled DNAzyme was furtherly explored by another gel electrophoresis (Supplementary Figure S3). The morphology of our R-HCR product was then examined by AFM. A substantial amount of micrometer-long linear dsDNA nanowires (~1.5 nm in diameter) was achieved for the analyte-triggered R-HCR machine (Figure 2D) while merely tiny spots of HCR monomers emerged for the non-triggered R-HCR system (Supplementary Figure S4), demonstrating our rational designed amplification system.

Feasibility of R-HCR system for amplified DNA detection

Additionally, the underlying molecular reaction mechanism of our engineered R-HCR system was explored by using computer-aided simulations after a sophisticated modeling of the system (details see the analytical modeling section of supporting information). The time-dependent fluorescence readout of the R-HCR system was then collected and furtherly subjected to the MATLab program through a non-linear regression procedure. A satisfied consistency between the simulated curves (solid lines) and experimental results (solid circles) was acquired as shown in Figure 3A. Supplementary Table S4 summarizes the as-achieved key parameters of each reaction scheme by using the reciprocal catalytic reaction model. Obviously, the R-HCR machinery is dominated by the lead-in HCR process (as revealed by its reaction rate constant K_T) and the DNAzyme biocatalysis process (as revealed by K_M and K_{cat}), which is reasonable since both of these two procedures are indispensable for carrying out the whole reaction processes. The comparably lower catalytic performance of the present HCR-reconstituted DNAzyme, as compared with the intact DNAzyme* (42), is attributed to the slightly varied microenvironment of DNAzyme structure. In addition, the present R-HCR system was demonstrated by the marginal signal leakage of HCR and DNAzyme, as demonstrated by their dramatically lower rate constants K_D and K_C. Interestingly, both of the sustained DNAzyme scission and efficient initiator exposure are needed to facilitate the high amplification performance of the present reciprocal replicating machinery. Noted that, even the side reaction or signal leakage (crosstalk from the intrinsic imperfection of reactants) is rather low, an obvious signal leakage could be predicted theoretically after a certainly prolonged reaction time from the simulations. These theoretical simulations show good coincidence with these experimental observations (Figure 3A). This also implies that the present R-HCR amplifier, in

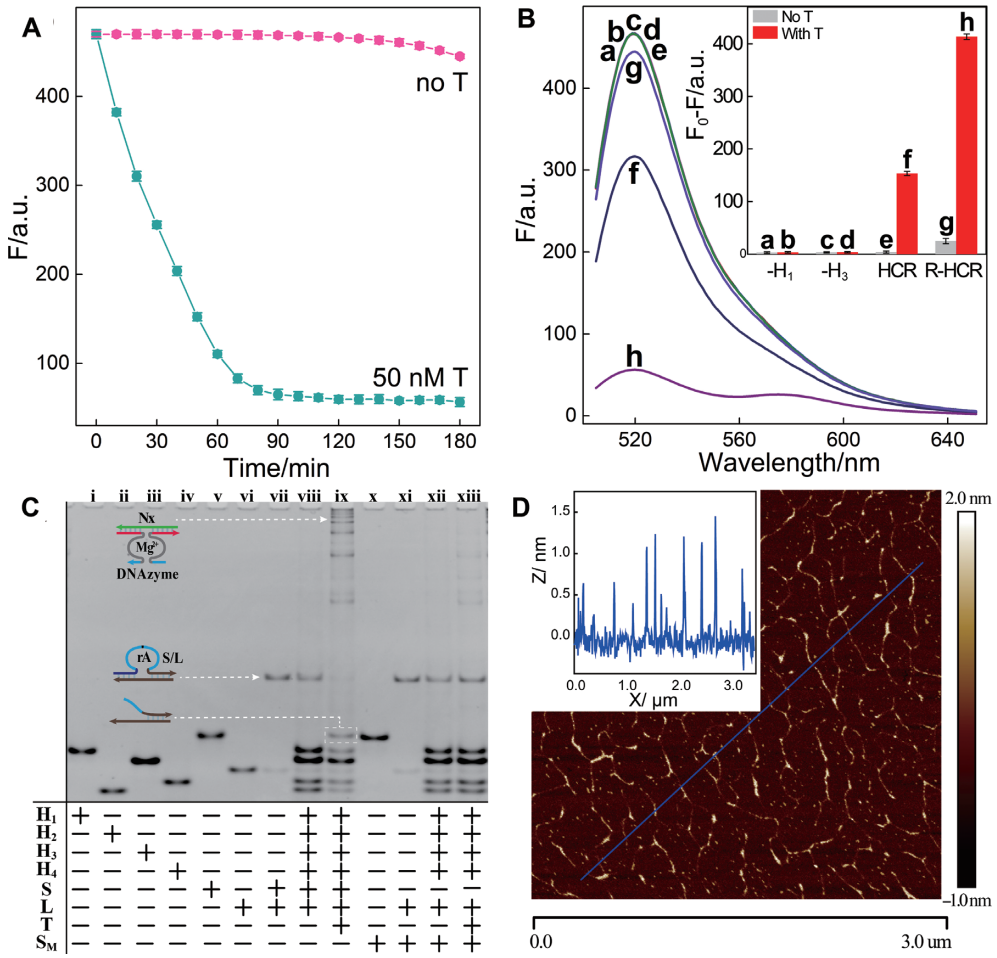

Figure 2. (**A**) Time-dependent fluorescence changes of the R-HCR system as shown in Figure 1 in the absence and presence of trigger **T**. (**B**) Fluorescence spectra of the triggered R-HCR system that was subtracted by $\mathbf{H_1}$ alone: (a) no **T**, (b) **T**; or by $\mathbf{H_3}$ alone: (c) no **T**, (d) **T**; $\mathbf{S_M}$-substituted R-HCR system: (e) no **T**, (f) **T**; and the intact R-HCR system: (g) no **T**, (h) **T**. Inset: Summary of the fluorescence intensity changes (at $\lambda = 520$ nm) shown in Figure 2B. (**C**) Native gel electrophoresis characterization of the R-HCR and conventional HCR systems. The '+' and '-' denote the presence and absence of the corresponding components, respectively. (**D**) AFM image and the cross-section analysis of the R-HCR-generated dsDNA nanowires. F_0 represents the original fluorescence intensity. Error bars were derived from $n = 5$ experiments.

principle, can detect analyte at single-molecule level, illuminating its powerful potential applications in bioanalytical fields.

Based on the aforementioned convincing results, it is clear that the R-HCR amplifier can be employed for sensitively analyzing trigger DNA. Accordingly, the fluorescence spectra of the R-HCR system were recorded after a fixed time interval of 3 h for analyzing different concentrations of trigger **T** (Figure 3B). Clearly, the fluorescence response intensified with increasing concentration of **T**. A low detection limit of 5.9 pM (3σ/slope) is acquired from the calibration curve (Figure 3B inset), which is comparable to and even lower than most of the other proteinase-free signal amplification methods (Supplementary Table S5). The performance of the $\mathbf{S_M}$-substituted R-HCR amplifier (as conventional HCR amplifier) was also employed for detecting the same trigger **T** (Figure 3C and Supplementary Figure S5). A tremendously lower FRET response was exhibited for the conventional HCR system (Figure 3C). The R-HCR amplifier shows a 78-fold signal enhancement than conventional HCR system, demonstrating the high signal gain of the present reciprocal catalytic amplifier. The selectivity of the R-HCR system was then evaluated by introducing one-, two-, or three-base mutant targets ($\mathbf{T_A}$, $\mathbf{T_B}$ and $\mathbf{T_C}$, respectively) (Figure 3D). The remarkable FRET readout of analyte **T** was easily discriminated from $\mathbf{T_A}$, $\mathbf{T_B}$ and $\mathbf{T_C}$, demonstrating the high selectivity of our R-HCR amplifier.

Versatility of R-HCR-sustained miR-21 and miR-155 visualization in living cells

Here the versatile reciprocal catalytic HCR-DNAzyme amplifier could be utilized as an amplification module, without further redesign and optimization of the entire system, for analyzing other targets through a facile integration with a sensing module. The modular feature of our sensing platform was demonstrated by choosing microRNA-21 (miR-21) as the model target. Abnormal miR-21 expressions are associated with a wide range of human cancers (44) and have been recognized as important indicators for cancer di-

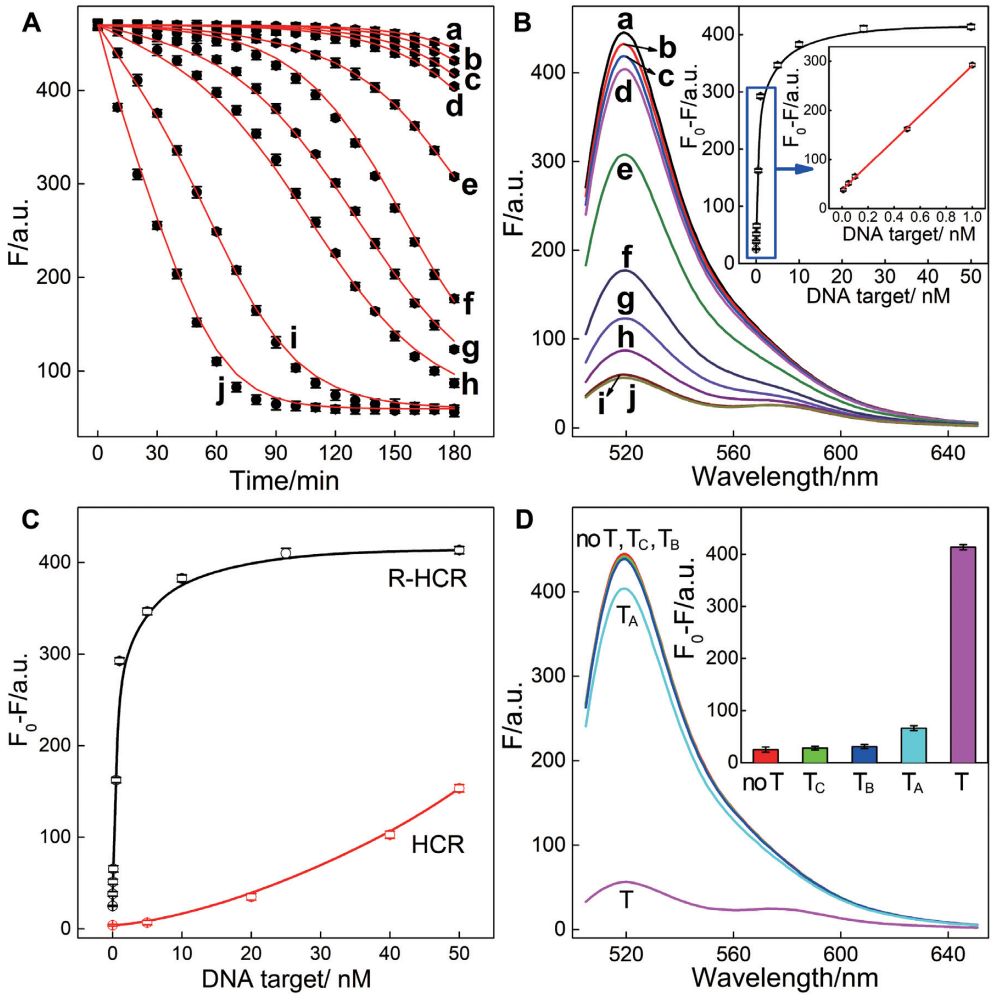

Figure 3. (**A**) Raw (solid circles) and simulated (line) time-dependent fluorescence changes of the R-HCR amplifier upon analysing different concentrations of target **T**. (**B**) Fluorescence spectra of the R-HCR machine activated by different concentrations of **T**: (a) 0, (b) 1×10^{-11}, (c) 5×10^{-11}, (d) 1×10^{-10}, (e) 5×10^{-10}, (f) 1×10^{-9}, (g) 5×10^{-9}, (h) 1×10^{-8}, (i) 2.5×10^{-8}, and (j) 5×10^{-8} M. Inset: resulting calibration curve. (**C**) Comparison of the R-HCR amplifier and conventional HCR system upon analyzing different concentrations of **T**. (**D**) Fluorescence spectra generated by the R-HCR amplifier upon analyzing different mutant analytes (50 nM). Inset: Summary of the fluorescence spectra as shown in Figure 3D.

agnosis and prognosis (45). As shown in Figure 5A, the sensing module includes only an auxiliary 'helper' hairpin $\mathbf{H_5}$ that is encoded with a miR-21-recognition sequence and a caged R-HCR initiator sequence (details, see Supplementary Figure S6). Target miR-21 can hybridize with $\mathbf{H_5}$ to expose a HCR trigger for motivating the R-HCR-accelerated FRET readout with satisfying low signal leakage (Figure 4A). The fluorescence spectra were acquired upon the analysis of different concentrations of miR-21 (Figure 4B). A detection limit of 6.8 pM was achieved for the R-HCR amplifier (Figure 4B inset). The selectivity of the miR-21 detection system was challenged by a series of interfering miRNAs: β-actin mRNA, son DNA and miR-122. A clear signal discrimination could be observed between miR-21 and these interfering strands, demonstrating the high specificity of the present miRNA assay (Figure 4C). Serum has little effect on the performance of the reciprocal catalytic amplifier, demonstrating its robust feature (Figure 4D). Thus the R-HCR machine can be developed as a general amplification tool for detecting low abundant analyte.

The satisfying anti-interference of the R-HCR system encouraged us to apply it as powerful intracellular imaging tool for visualizing analytes in living cells. Then the R-HCR amplifier was utilized to investigate the distinct miR-21 expressions of different cells by using confocal laser scanning microscopy (CLSM). Here, all DNA probes were partially modified with phosphorothioate bonds to prevent the potential nuclease degradation in living cells (details see Supplementary Table S2). The performance of phosphorothioate R-HCR system shows a good agreement with that of the intact R-HCR system (Supplementary Figure S7), indicating such modification has little effect on their sensing performance. The low cytotoxicity of the R-HCR system was demonstrated by a conventional MTT assay *in vitro* (Supplementary Figure S8). Considering the unexpectedly distinct and complex intracellular environment of different cells, the fluorescence emission ratio of acceptor to donor (F_A/F_D) was employed as a visualization readout to minimize the undesired system fluctuations. Our proposed R-HCR was adapted for intracellular miR-21 imaging in three

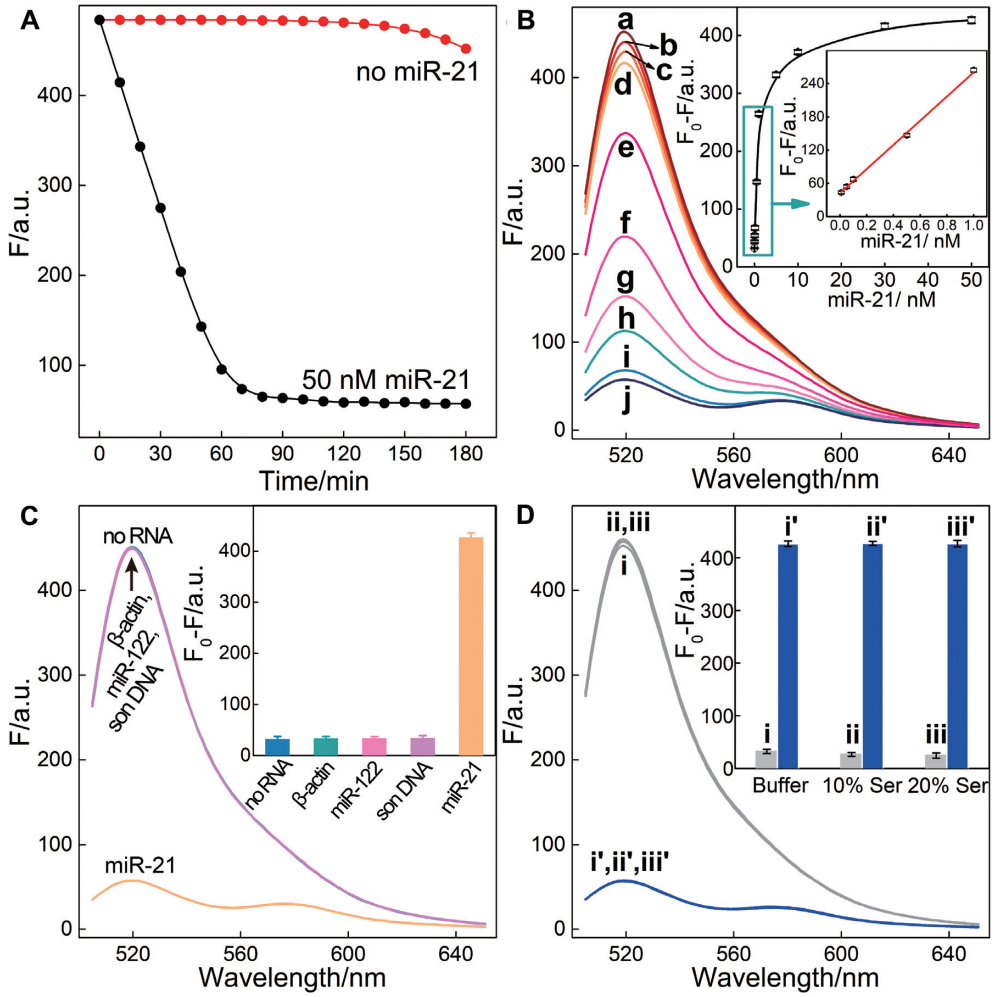

Figure 4. (**A**) Time-dependent fluorescence changes of the updated R-HCR system with and without miR-21. (**B**) Fluorescence spectra of the miR-21-targeting R-HCR sensing platform generated by different concentrations of miR-21 after 3 h: (a) 0, (b) 1×10^{-11}, (c) 5×10^{-11}, (d) 1×10^{-10}, (e) 5×10^{-10}, (f) 1×10^{-9}, (g) 5×10^{-9}, (h) 1×10^{-8}, (i) 3×10^{-8}, and (j) 5×10^{-8} M. Inset: resulting calibration curve. (**C**) Fluorescence spectra generated by the updated R-HCR amplifier upon analysing different analytes (50 nM). Inset: Summary of the fluorescence spectra as shown in (C). (**D**) Fluorescence spectra generated by the updated R-HCR system upon analyzing 50 nM of miR-21 in different serum solutions: buffer without (i) and with (i') miR-21, 10% serum without (ii) and with (ii') miR-21, 20% serum without (iii) and with (iii') miR-21. Inset: Summary of the fluorescence spectra as shown in (D). Error bars were derived from n = 5 experiments.

different types of cell lines, including human breast cancer (MCF-7) with relatively high miR-21 expression profile, human cervical cancer cells (HeLa) with relatively low miR-21 expression profile, and human embryonic lung fibroblast cells (MRC-5) with no miR-21 expression. The R-HCR-mediated intracellular imaging system was transfected into these different living cells via lipofectamine 3000 for 4 h (an optimized incubation time, see Supplementary Figure S9). An extremely intense FRET signal of miR-21 target was observed in MCF-7 cells (sample a, Figure 5B) while a comparatively weaker FRET response emerged in HeLa cells (sample e, Figure 5B). In contrast, no detectable FRET signal appeared in MRC-5 cells (sample f, Figure 5B), indicating a higher expression of miR-21 in tumor cells than normal cells, which was accordant with the previous report (24,46). The FRET signal of MCF-7 cells was 3.0- and 26.1-fold higher than that of HeLa cells and MRC-5 cells (Figure 5D), which was consistent with conventional qRT-PCR assay (Supplementary Figure S10 and Table S3). Thus the reciprocal R-HCR imaging platform provided precise localization of miR-21 in living cells. Moreover, a substantially declined FRET signal appeared in MCF-7 cells that were pretreated with anti-miRNA antisense inhibitor oligonucleotide (sample c of Figure 5B), implying that the miR-21 molecules were indeed presented in MCF-7 cells for activating the R-HCR system. The corresponding scatter plot of FRET signal furtherly evidenced the highly powerful intracellular biosensing performance of our R-HCR amplifier (Figure 5C). A statistical histogram analysis of the FRET signal (F_A/F_D) of the R-HCR imaging system was collected as shown in Figure 5D. The FRET efficiency of the R-HCR imaging system was acquired to be 0.63 by using conventional acceptor-photo-bleaching method (Supplementary Figure S11). Overall, the R-HCR imaging system enables a reliable discrimination of different miR-21 expressions in living cells.

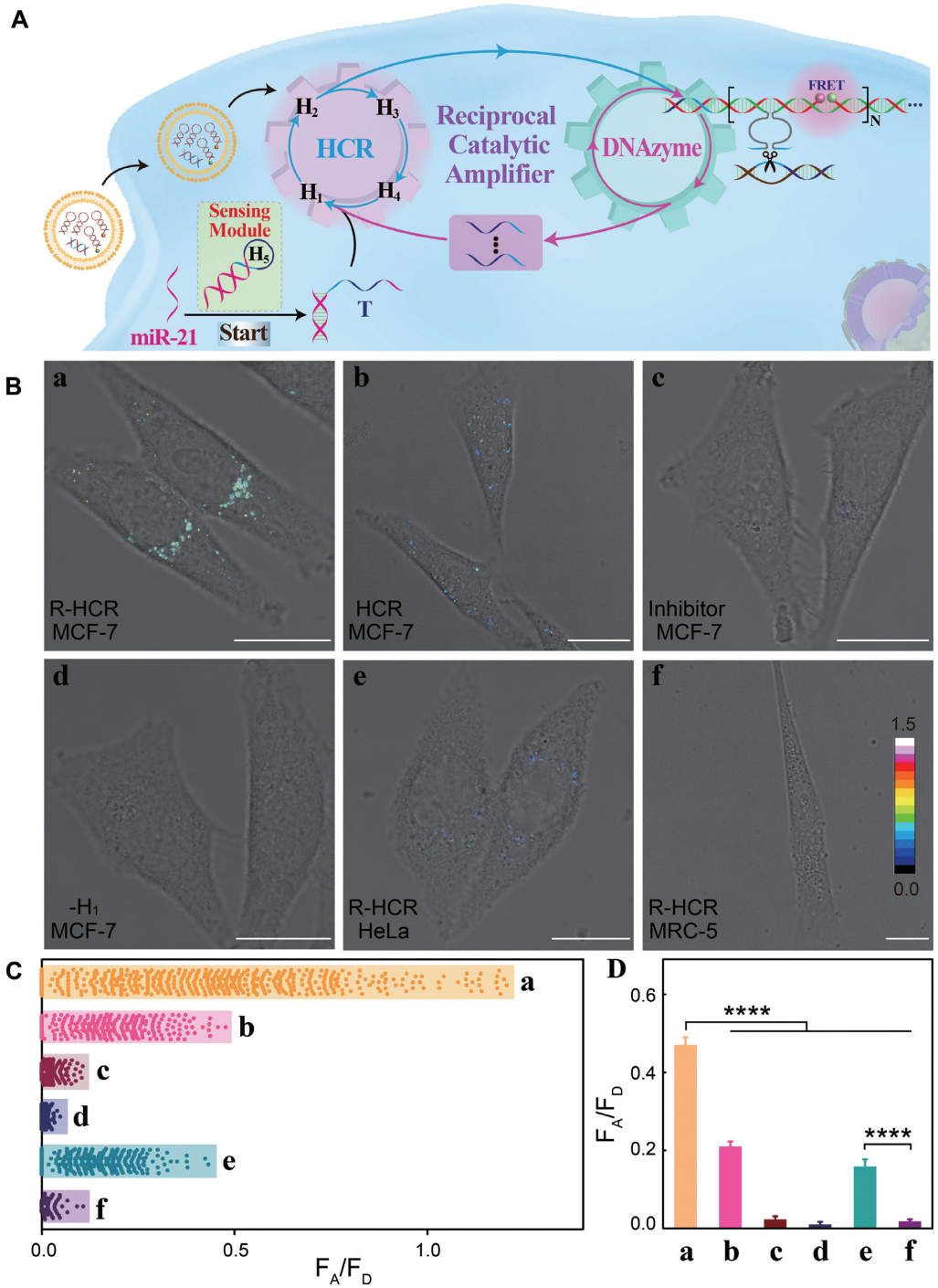

Figure 5. (**A**) Schematic representation of the miR-21-targeting R-HCR sensing platform by introducing a foreign helper $\mathbf{H_5}$ into the well-established R-HCR amplifier. (**B**) Intracellular analysis of miR-21 based on the updated R-HCR imaging system and FRET transduction (in the form of F_A/F_D). CLSM probing of intracellular miR-21 by (a) R-HCR amplifier in MCF-7 cells, (b) conventional HCR amplifier in MCF-7 cells, (c) R-HCR amplifier with a chemically modified miR-21 inhibitor in MCF-7 cells, (d) $\mathbf{H_1}$-expelled R-HCR amplifier in MCF-7 cells, (e) R-HCR amplifier in HeLa cells, and (f) R-HCR amplifier in MRC-5 cells. All scale bars correspond to 20 μm. (**C**) The acquired FRET signal (F_A/F_D) distributions from Figure 5B. (**D**) Statistical histogram analysis of the FRET signal (F_A/F_D) of these different cell samples through the R-HCR imaging system.

Furthermore, the intracellular miR-21 localization was demonstrated by 3D z-stack projections through integrating a series of z-section images of the entire cells (Supplementary Figure S12, Supplementary video S1). Clearly, the endogenous miR-21 is distributed in the cytoplasm of MCF-7 cells, demonstrating that our R-HCR imaging system realized the spatially resolved intracellular miRNA visualization. The mutually reinforcing replication between the transducer HCR and DNAzyme biocatalyst was similarly verified by excluding one of the non-fluorescent hairpin reactants or by replacing the mutant substrate ($\mathbf{S_M}$) from the R-HCR imaging mixture. As compared with the intact R-HCR imaging system (sample a of Supplementary Figure S13A), almost no FRET readout was shown in MCF-7 cells that were transfected with $\mathbf{H_1}$- or $\mathbf{H_3}$-expelled R-HCR imaging system (sample c, d of Supplementary Figure S13A, respectively) while a weak FRET response emerged in MCF-7 cells that were transfected with the $\mathbf{S_M}$-substituted R-HCR system (sample b of Figure 5B and Supplementary Figure S13A). As compared with traditional HCR system, the R-HCR machine lead to the generation of more dsDNA nanowires and more efficient FRET imaging signal for analyzing miRNA in living cells. These demonstrated that each of these amplification constitutes was indispensable for carrying out the synergistically amplified sensing platform, which was consistent with previous *in vitro* studies (Figure 2B). In our design, the updated R-HCR system recognized and hybridized miR-21 to form stable complexes, which would lead to the upregulation of the downstream target genes of PDCD4 and PTEN. A distinct up-regulated PDCD4 and PTEN mRNAs/proteins was presented in R-HCR system or miR-21 inhibitor-treated MCF-7 cells (Supplementary Figure S14), indicating the specific binding of the R-HCR probe with miR-21 inside living cells.

Encouraged by these results, we further validated the generality of our R-HCR strategy only by updating the accessorial sensing module $\mathbf{H_6}$ for another microRNA, miR-155, which is sufficient to induce tumorigenesis. High expression of miRNA-155 has been reported in various B cell malignancies (47). Benefiting from the modular design, the miRNA-155-detecting R-HCR system can be readily constructed only by re-encoding hairpin $\mathbf{H_6}$ with a miR-155-recognition sequence and a caged R-HCR initiator sequence (Supplementary Figure S15). As shown in Figure 6A, miR-155 opens $\mathbf{H_6}$ to release HCR trigger for stimulating the R-HCR-amplified FRET response. The fluorescence spectra of the updated R-HCR system were obtained upon its incubation with various concentrations of miRNA-155 (Figure 6B). A good linear relationship was acquired between fluorescence change and miRNA-155 concentration ranging from 10 pM to 1 nM (Figure 6B inset). The limit of detection (LOD) was calculated to be 7.6 pM based on the 3σ method. Three different interfering miRNAs (β-actin mRNA, miR-122 and miR-21) were chosen to further examine the specificity of the updated R-HCR system toward miRNA-155. As shown in Figure 6C, the R-HCR system showed low FRET response toward these interfering miRNAs, which were close to the blank control. These results indicated that this proposed method had high specificity for miRNA detection in complex cellular environment.

Based on the above results, we applied the R-HCR amplifier to investigate the varied expressions of miR-155 in human lung cancer (A549), human cervical cancer cells (HeLa) and human embryonic lung fibroblast cells (MRC-5) by using CLSM technique. It was found that the average FRET signal per cell decreases in the order of A549 cells > HeLa cells > MRC-5 cells (samples a, e and f of Figure 6D), which is consistent with previous research (48), suggesting the good capability of the R-HCR imaging platform for precise localization of low-abundance miR-155 in different living cells. Moreover, a significantly decreased FRET signal was exhibited in the anti-miRNA-treated A549 cells (sample c of Figure 6D), demonstrating that the R-HCR imaging system enables a reliable sensing of miR-155 in living cells. To verify the in situ enhanced amplification capability of our R-HCR machinery in living cells, control experiments were performed by expelling one of the non-fluorescent hairpin reactants or replacing the substrate ($\mathbf{S}$) with the mutant substrate ($\mathbf{S_M}$). As shown in Figure 6D, a negligible FRET signal was observed in A549 cells that were treated with $\mathbf{H_1}$-expelled R-HCR imaging system (sample d, Figure 6D) while a faint FRET response was exhibited in A549 cells treated with the $\mathbf{S_M}$-substituted R-HCR system (conventional HCR amplifier, sample b, Figure 6D). Obviously, the R-HCR machinery leads to the generation of more DNAzyme nanowires and more efficient FRET imaging signal for monitoring miRNA in living cells (sample a, Figure 6D). The corresponding scatter plot of FRET signal distribution was exhibited in Figure 6E and a statistical histogram analysis of the FRET signal (F_A/F_D) of the R-HCR imaging system was shown in Figure 6F. These results evidenced the versatile and reliable intracellular imaging performance of our R-HCR amplifier.

In vivo miR-21 imaging by the R-HCR system

Inspired by the excellent intracellular visualization performance *in vitro*, we further examined the updated R-HCR system for miRNA imaging *in vivo*. Hairpin $\mathbf{H_4}$ was modified with a Cy5/quencher pair for miR-21 bioimaging. The biocompatibility of R-HCR system was further demonstrated by hemolysis test (Supplementary Figure S16), hematology and biochemical analysis (Supplementary Figure S17), and H&E staining assay (Supplementary Figure S18). The intratumoral imaging performance of the R-HCR amplifier was first explored by intratumoral injection of nude mice bearing subcutaneous MCF-7 tumor on the right back. Upon exciting the mice with a fixed excitation wavelength (λ_{ex} = 640 nm), the fluorescence signal reached its maximum value at 6 h postinjection of lipo3000-loaded R-HCR mixture and then decreased (Figure 7A). Quantitative analysis showed that R-HCR-treated mice presented 2.0- and 3.5-fold higher intratumoral Cy5 signal than that treated with HCR and $\mathbf{H_5}$-excluded R-HCR systems at 6 h (Figure 7B). Furthemore, the miRNA-21 inhibitor was injected into tumor site for knocking down miR-21 expression, as expected, scarcely any Cy5 signal was observed at miRNA-21 inhibitor-pretreated tumor, showing good agreement with the cellular experiments. Addi-

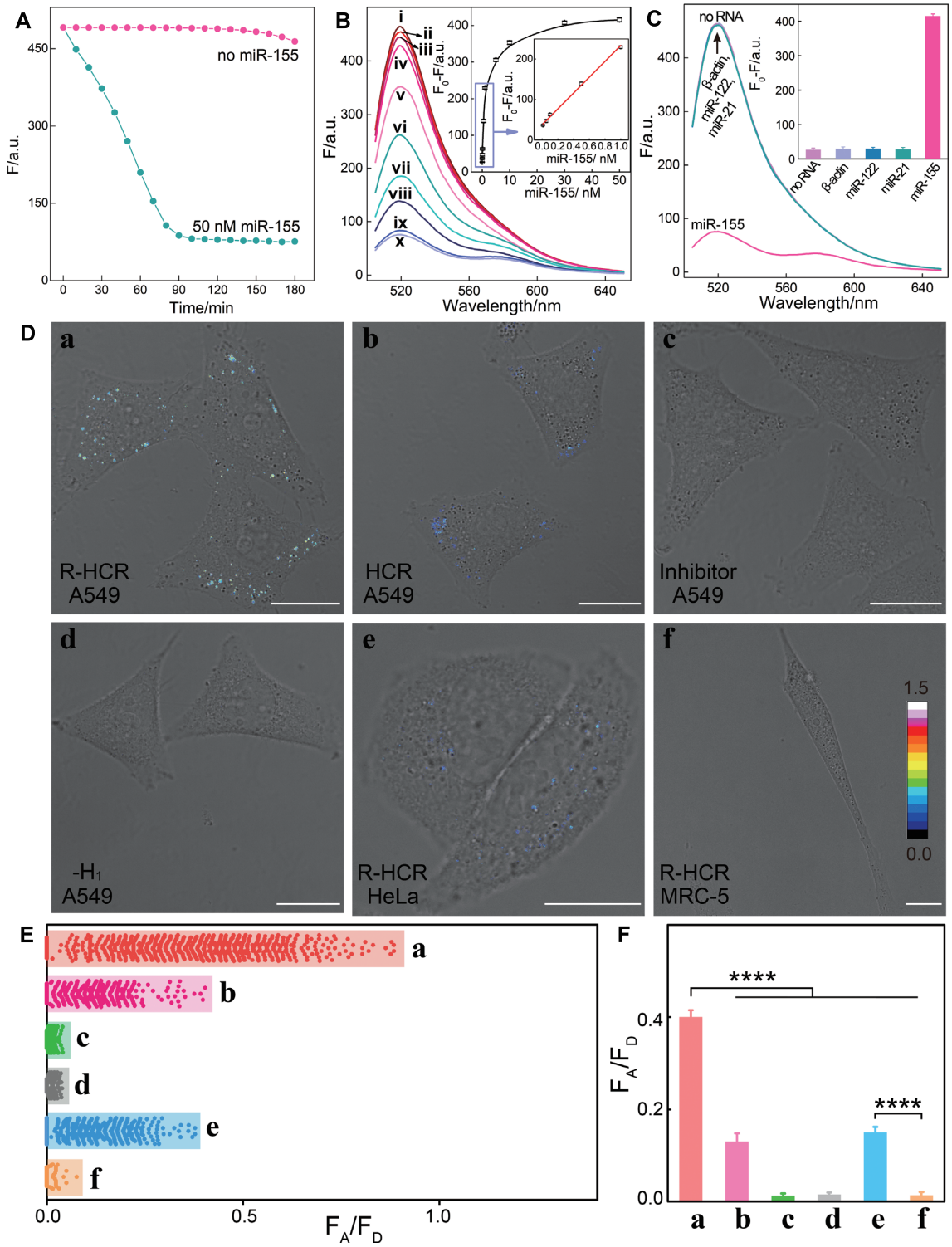

Figure 6. (**A**) Time-dependent fluorescence changes of the miR-155-targeting R-HCR sensing platform without and with miR-155. (**B**) Fluorescence spectra of the R-HCR system generated by different concentrations of miR-155 after 3 h: (i) 0, (ii) 1×10^{-11}, (iii) 5×10^{-11}, (iv) 1×10^{-10}, (v) 5×10^{-10}, (vi) 1×10^{-9}, (vii) 5×10^{-9}, (viii) 1×10^{-8}, (ix) 3×10^{-8} and (x) 5×10^{-8} M. Inset: resulting calibration curve. (**C**) Fluorescence spectra of the R-HCR amplifier upon analysing different interfering analytes (50 nM). Inset: Summary of the fluorescence spectra. Error bars were derived from n = 5 experiments. (**D**) Intracellular analysis of miR-155 through the R-HCR imaging system and FRET transduction (in the form of F_A/F_D). CLSM probing of intracellular miR-155 by (a) R-HCR in A549 cells, (b) conventional HCR in A549 cells, (c) R-HCR with a chemically modified miR-155 inhibitor in A549 cells, (d) $\mathbf{H_1}$-expelled R-HCR in A549 cells, (e) R-HCR in HeLa cells and (f) R-HCR in MRC-5 cells. All scale bars correspond to 20 μm. (**E**) The acquired FRET signal (F_A/F_D) distributions from (D). (**F**) Statistical histogram analysis of the FRET signal (F_A/F_D) of these different cell samples through the R-HCR imaging system.

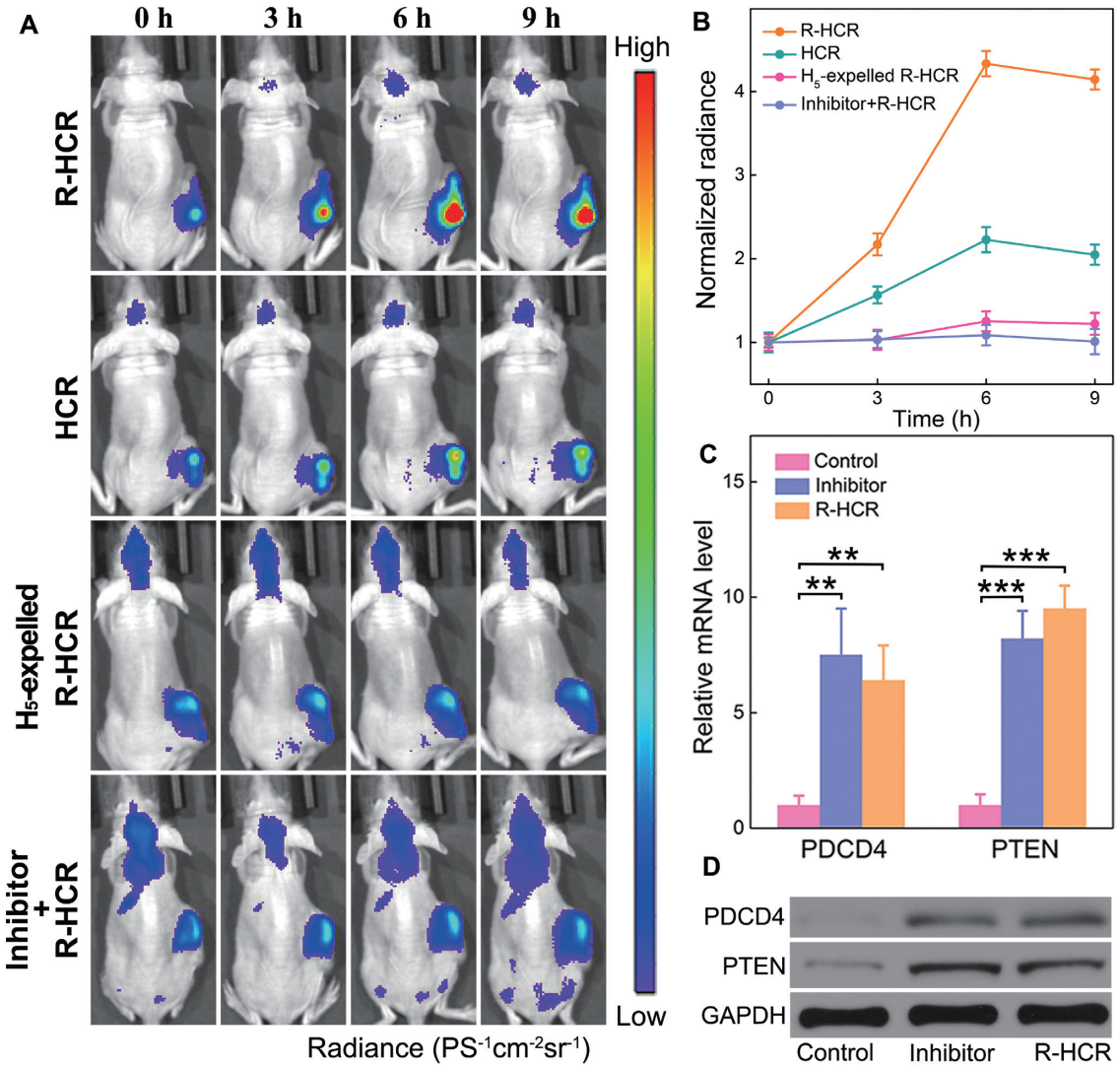

Figure 7. The R-HCR-activated miRNA imaging in tumors by intratumoral injection. (**A**) Whole-body fluorescence imaging of MCF-7 tumor-bearing mice after injection of R-HCR, HCR, **H5**-expelled R-HCR and R-HCR amplifier with a chemically modified miR-21 inhibitor. (**B**) Quantification of the fluorescence of tumor sites in (A). (**C**) qRT-PCR and (**D**) western blot analysis of PDCD4 and PTEN in mice tumor after intratumoral injection of PBS, miR-21 inhibitor and R-HCR system.

tionally, a significant enhancement of PDCD4 and PTEN mRNAs/proteins was shown in mice tumor that was treated with the updated R-HCR system or miR-21 inhibitor (Figure 7C and 7D), which was consistent with the corresponding cellular studies. Thus the R-HCR system could realize miRNA-21 imaging in living mice.

We further examined the imaging performance of the R-HCR imaging system in living mice bearing MCF-7 tumor by tail vein injection (Supplementary Figure S19A). The lipo3000-loaded R-HCR system could gradually accumulate in tumor site via EPR effect. Quantitative analysis showed that the R-HCR group displayed 2.2- and 3.4-fold higher intratumoral Cy5 signal than the HCR and **H5**-excluded R-HCR groups at 12 h (Supplementary Figure S19B). The enhanced Cy5 signal of R-HCR in tumors was attributed to the reciprocal reinforcement feature of HCR and DNAzyme biocatalysis that accelerated the entire reaction procedure and promoted the generation of an amplified Cy5 signal. Furthermore, the Cy5 of harvested tumors and organs at 12 h post-injection was analyzed (Supplementary Figures S19C and S19D). The intratumoral Cy5 signal in the R-HCR group was 3.3- and 4.6-fold higher than that in HCR and the **H5**-excluded R-HCR groups, respectively. Additionally, the Cy5 of normal organs revealed no distinct difference for all groups, proving the precise miRNA imaging in living mice.

DISCUSSION

An unprecedented reciprocal replicating DNA machine was engineered for high-performance *in vivo* miRNA imaging based on the synergistic cross-activation of HCR and DNAzyme procedures. Target-activated transducer HCR assembles long tandem DNAzyme nanowires, which catalyze the cyclic and continuous generation of triggers for reversely feeding back HCR transducer. The flexible

DNAzyme design dictates a more facile assembly of HCR machine while the high catalytic efficiency of DNAzyme contributes to the utmost in-depth amplification. Our DNAzyme utilizes endogenous Mg^{2+} ions as the indispensable DNAzyme cofactors without additional DNAzyme cofactors, which is more easier for machinery design and operation. This cross-invasion of transducer HCR and DNAzyme biocatalysis could convert the limited molecular recognition event into an efficient accumulation of amplicons as well as the remarkable FRET motivation. The underlying molecular-level propagation mechanism of the R-HCR machine, especially the comprising HCR and DNAzyme biocatalysis reactions, was systematically examined by experimental studies and computer-aided simulations after an appropriate modeling of the system. Given the accelerated reaction format and the multiple-guaranteed recognitions, the proteinase-free DNA machine was successfully applied to sensitively and selectively detect target. This robust amplifier could be easily integrated with a general and versatile sensing module for realizing an accurate miRNA localization with high reliability in living cells and even living mice through a facile fluorescence imaging technique, thus provides a powerful sensing platform for tracing low-amount biomarkers *in vivo*. As a nanomaterial-free sensing platform, our system could avoid the unexpected adverse retention of transfecting inorganic nanomaterials *in vivo* and the accompanying unexpected biotoxicity. The R-HCR machine holds great potential for clinical diagnosis and therapeutic evaluation.

SUPPLEMENTARY DATA

Supplementary Data are available at NAR Online.

FUNDING

Natural Science Foundation of China [21874103, 81602610]; National Basic Research Program of China (973 Program) [2015CB932601]; Fundamental Research Funds for the Central Universities [2042018kf0210, 2042019kf0206]. Funding for open access charge: National Basic Research Program of China (973 Program) [2015CB932601].
Conflict of interest statement. None declared.

REFERENCES

1. Zhang,H., Li,F., Dever,B., Li,X.F. and Le,X.C. (2013) DNA-mediated homogeneous binding assays for nucleic acids and proteins. *Chem. Rev.*, **113**, 2812–2841.
2. Duan,R., Lou,X. and Xia,F. (2016) The development of nanostructure assisted isothermal amplification in biosensors. *Chem. Soc. Rev.*, **45**, 1738–1749.
3. Guo,S. and Wang,E. (2011) Functional micro/nanostructures: simple synthesis and application in sensors, fuel cells, and gene delivery. *Acc. Chem. Res.*, **44**, 491–500.
4. Jung,C. and Ellington,A.D. (2014) Diagnostic applications of nucleic acid circuits. *Acc. Chem. Res.*, **47**, 1825–1835.
5. Gill,P. and Ghaemi,A. (2008) Nucleic acid isothermal amplification technologies-a review. *Nucleosides Nucleotides Nucleic Acids*, **27**, 224–243.
6. Banér,J., Nilsson,M., Mendel-Hartvig,M. and Landegren,U. (1998) Signal amplification of padlock probes by rolling circle replication. *Nucleic Acids Res.*, **26**, 5073–5078.
7. Notomi,T., Okayama,H., Masubuchi,H., Yonekawa,T., Watanabe,K., Amino,N. and Hase,T. (2000) Loop-mediated isothermal amplification of DNA. *Nucleic Acids Res.*, **28**, e63.
8. Walker,G.T., Fraiser,M.S., Schram,J.L., Little,M.C., Nadeau,J.G. and Malinowski,D.P. (1992) Strand displacement amplification-an isothermal, *in vitro* DNA amplification technique. *Nucleic Acids Res.*, **20**, 1691–1696.
9. Willner,I., Shlyahovsky,B., Zayats,M. and Willner,B. (2008) DNAzymes for sensing, nanobiotechnology and logic gate applications. *Chem. Soc. Rev.*, **37**, 1153–1165.
10. Zhang,D.Y. and Seelig,G. (2011) Dynamic DNA nanotechnology using strand-displacement reactions. *Nat. Chem.*, **3**, 103–113.
11. Wang,Z.-G., Zhan,P. and Ding,B. (2013) Self-assembled catalytic DNA nanostructures for synthesis of para-directed polyaniline. *ACS Nano*, **7**, 1591–1598.
12. Liu,J. and Lu,Y. (2007) A DNAzyme catalytic beacon sensor for paramagnetic Cu^{2+} ions in aqueous solution with high sensitivity and selectivity. *J. Am. Chem. Soc.*, **129**, 9838–9839.
13. Wang,Y. and Irudayaraj,J. (2011) A SERS DNAzyme biosensor for lead ion detection. *Chem. Commun.*, **47**, 4394–4396.
14. Wang,F., Elbaz,J. and Willner,I. (2012) Enzyme-free amplified detection of DNA by an autonomous ligation DNAzyme machinery. *J. Am. Chem. Soc.*, **134**, 5504–55007.
15. Liu,M., Zhang,Q., Chang,D., Gu,J., Brennan,J.D. and Li,Y. (2017) A DNAzyme feedback amplification strategy for biosensing. *Angew. Chem. Int. Ed.*, **129**, 6238–6242.
16. Wang,F., Elbaz,J., Teller,C. and Willner,I. (2011) Amplified detection of DNA through an autocatalytic and catabolic DNAzyme-Mediated process. *Angew. Chem. Int. Ed.*, **50**, 295–299.
17. Tian,Y., He,Y., Chen,Y., Yin,P. and Mao,C. (2005) A DNAzyme that walks processively and autonomously along a One-Dimensional track. *Angew. Chem. Int. Ed.*, **44**, 4355–4358.
18. Peng,H., Li,X.-F., Zhang,H. and Le,X.C. (2017) A microRNA-initiated DNAzyme motor operating in living cells. *Nat. Commun.*, **8**, 14378.
19. Dirks,R.M. and Pierce,N.A. (2004) Triggered amplification by hybridization chain reaction. *Proc. Natl. Acad. Sci. USA*, **101**, 15275–15278.
20. Choi,H.M.T., Chang,J.Y., Trinth,L.A., Padilla,J.E., Frase,S.E. and Pierce,N.A. (2010) Programmable *in situ* amplification for multiplexed imaging of mRNA expression. *Nat. Biotechnol.*, **28**, 1208–1212.
21. Choi,H.M.T., Beck,V.A. and Pierce,N.A. (2014) Next-generation *in situ* hybridization chain reaction: higher gain, lower cost, greater durability. *ACS Nano*, **8**, 4284–4294.
22. Wu,Z., Liu,G.Q., Yang,X.L. and Jiang,J.H. (2015) Electrostatic nucleic acid nanoassembly enables hybridization chain reaction in living cells for ultrasensitive mRNA imaging. *J. Am. Chem. Soc.*, **137**, 6829–6836.
23. Huang,J., Wu,Y., Chen,Y., Zhu,Z., Yang,X., Yang,C.J., Wang,K. and Tan,W. (2011) Pyrene-excimer probes based on the hybridization chain reaction for the detection of nucleic acids in complex biological fluids. *Angew. Chem. Int. Ed.*, **50**, 401–404.
24. Cheglakov,Z., Cronin,T.M., He,C. and Weizmann,Y. (2015) Live cell microRNA imaging using cascade hybridization reaction. *J. Am. Chem. Soc.*, **137**, 6116–6119.
25. Yang,L., Liu,C.H., Ren,W. and Li,Z.P. (2012) Graphene surface-anchored fluorescence sensor for sensitive detection of microRNA coupled with enzyme-free signal amplification of hybridization chain reaction. *ACS Appl. Mater. Interfaces*, **4**, 6450–6453.
26. Wei,J., Gong,X., Wang,Q., Pan,M., Liu,X., Liu,J., Xia,F. and Wang,F. (2018) Construction of an autonomously concatenated hybridization chain reaction for signal amplification and intracellular imaging. *Chem. Sci.*, **9**, 52–61.
27. Wang,F., Elbaz,J., Orbach,R., Magen,N. and Willner,I. (2011) Amplified analysis of DNA by the autonomous assembly of polymers consisting of DNAzyme wires. *J. Am. Chem. Soc.*, **133**, 17149–17151.
28. Li,B., Jiang,Y., Chen,X. and Ellington,A.D. (2012) Probing spatial organization of DNA strands using enzyme-free hairpin assembly circuits. *J. Am. Chem. Soc.*, **134**, 13918–13921.
29. Zhou,Y., Yang,L., Wei,J., Ma,K., Gong,X., Shang,J., Yu,S. and Wang,F. (2019) An autonomous nonenzymatic concatenated DNA circuit for amplified imaging of intracellular ATP. *Anal. Chem.*, **91**, 15229–15234.

30. Wang,H., Wang,H., Wu,Q., Liang,M., Liu,X. and Wang,F. (2019) A DNAzyme-amplified DNA circuit for highly accurate microRNA detection and intracellular imaging. *Chem. Sci.*, **10**, 9597–9604.
31. Gong,X., Wei,J., Liu,J., Li,R., Liu,X. and Wang,F. (2019) Programmable intracellular DNA biocomputing circuits for reliable cell recognitions. *Chem. Sci.*, **10**, 2989–2997.
32. Kausar,A., McKay,R.D., Lam,J., Bhogal,R.S., Tang,A.Y. and Gibbs-Davis,J.M. (2011) Tuning DNA stability to achieve turnover in template for an enzymatic ligation reaction. *Angew. Chem. Int. Ed.*, **50**, 8922–8926.
33. Kausar,A., Mitran,C.J., Li,Y. and Gibbs-Davis,J.M. (2013) Rapid, isothermal DNA self-replication induced by a destabilizing lesion. *Angew. Chem. Int. Ed.*, **52**, 10577–10581.
34. Nie,J., Zhao,M. Z, Xie,W.J., Cai,L.Y., Zhou,Y.L. and Zhang,X.X. (2015) DNA cross-triggered cascading self-amplification artificial biochemical circuit. *Chem. Sci.*, **6**, 1225–1229.
35. Lincoln,T.A. and Joyce,G.F. (2009) Self-sustained replication of an RNA enzyme. *Science*, **323**, 1229–1232.
36. Levy,M. and Ellington,A.D. (2003) Exponential growth by cross-catalytic cleavage of deoxyribozymogens. *Proc. Natl. Acad. Sci. U.S.A.*, **100**, 6416–6421.
37. Yang,L., Wu,Q., Chen,Y., Liu,X., Wang,F. and Zhou,X. (2019) Amplified MicroRNA detection and intracellular imaging based on an autonomous and catalytic assembly of DNAzyme. *ACS Sens.*, **4**, 110–117.
38. Wu,Q., Wang,H., Gong,K., Shang,J., Liu,X. and Wang,F. (2019) Construction of an autonomous nonlinear hybridization chain reaction for extracellular Vesicles-Associated MicroRNAs discrimination. *Anal. Chem.*, **91**, 10172–10179.
39. Wang,H., Li,C., Liu,X., Zhou,X. and Wang,F. (2018) Construction of an enzyme-free concatenated DNA circuit for signal amplification and intracellular imaging. *Chem. Sci.*, **9**, 5842–5849.
40. Wei,J., Wang,H., Wu,Q., Gong,X., Ma,K., Liu,X. and Wang,F. (2020) A smart autocatalytic DNAzyme biocircuit for in vivo amplified MicroRNA imaging. *Angew. Chem. Int. Ed.*, **59**, 5965–5971.
41. Wu,C., Cansiz,S., Zhang,L., Teng,I.T., Qiu,L., Li,J., Liu,Y., Zhou,C., Hu,R., Zhang,T. *et al.* (2015) A nonenzymatic hairpin DNA cascade reaction provides high signal gain of mRNA imaging inside live cells. *J. Am. Chem. Soc.*, **137**, 4900–4903.
42. Breaker,R.R. and Joyce,G.F. (1995) A DNA enzyme with Mg^{2+}-Dependent RNA phosphoesterase activity. *Chem. Biol.*, **2**, 655–660.
43. Zadeh,J.N., Steenberg,C.D., Bois,J.S., Wolfe,B.R., Pierce,M.B., Khan,A.R., Dirks,R.M. and Pierce,N.A. (2011) NUPACK: analysis and design of nucleic acid systems. *J. Comput. Chem.*, **32**, 170–173.
44. Bartel,D.P. (2004) MicroRNAs: genomics, biogenesis, mechanism, and function. *Cell*, **116**, 281–297.
45. Calin,G.A. and Croce,C.M. (2006) MicroRNA signatures in human cancers. *Nat. Rev. Cancer*, **6**, 857–866.
46. Liang,C.P., Ma,P.Q., Liu,H., Guo,X.G., Yin,B.C. and Ye,B.C. (2017) Rational engineering of a dynamic, entropy-driven DNA nanomachine for intracellular microRNA imaging. *Angew. Chem. Int. Ed.*, **56**, 9077–9081.
47. Eis,P.S., Tam,W., Sun,L., Chadburn,A., Li,Z., Gomez,M.F., Lund,E. and Dahlberg,J.E. (2005) Accumulation of miR-155 and *BIC* RNA in human B cell lymphomas. *Proc. Natl. Acad. Sci. USA*, **102**, 3627–3632.
48. Lee,H., Park,J.-E. and Nam,J.-M. (2014) Bio-barcode gel assay for microRNA. *Nat. Commun.*, **5**, 3367.